The Astrophysical Journal, 914:26 (10pp), 2021 June 10 https://doi.org/10.3847/1538-4357/abf8b1
© 2021. The American Astronomical Society. All rights reserved.

Microscale Processes Determining Macroscale Evolution of Magnetic Flux Tubes along Earth's Magnetopause

K.-J. Hwang[1], J. L. Burch[1], C. T. Russell[2], E. Choi[1], K. Dokgo[1], R. C. Fear[3], S. A. Fuselier[1], S. M. Petrinec[4], D. G. Sibeck[5], H. Hasegawa[6], H. Fu[7], M. Øieroset[8], C. P. Escoubet[9], B. L. Giles[5], Y. Khotyaintsev[10], D. B. Graham[10], D. J. Gershman[5], C. J. Pollock[11], R. E. Ergun[12], R. B. Torbert[13], and J. Broll[14]

[1] Southwest Research Institute, San Antonio, TX, USA; jhwang@swri.edu
[2] Institute of Geophysics and Planetary Physics, University of California, Los Angeles, CA, USA
[3] University of Southampton, Southampton, UK
[4] Lockheed Martin Advanced Technology Center, Palo Alto, CA 94304, USA
[5] NASA Goddard Space Flight Center, Greenbelt, MD, USA
[6] Institute of Space and Astronautical Science, Japan Aerospace Exploration Agency, Sagamihara, Japan
[7] School of Science and Environment, Beihang University, Beijing, People's Republic of China
[8] Space Sciences Laboratory, University of California, Berkeley, Berkeley, CA, USA
[9] European Space Agency, The Netherlands
[10] Swedish Institute of Space Physics, Uppsala, Sweden
[11] Denali Scientific, LLC, Fairbanks, AK, USA
[12] Laboratory for Atmospheric and Space Physics, University of Colorado at Boulder, Boulder, CO, USA
[13] Space Science Center, University of New Hampshire, Durham, NH, USA
[14] Center for Space Physics, Boston University, Boston, MA, USA
Received 2021 February 22; revised 2021 March 29; accepted 2021 April 14; published 2021 June 10

Abstract

An important process affecting solar wind–Earth's magnetosphere coupling is nonsteady dayside magnetic reconnection, observationally evidenced by a flux transfer event (FTE) that shows a bipolar variation of the magnetic field component normal to the magnetopause. FTEs often consist of two interlinked flux tubes, but, local kinetic processes between the flux tubes are not understood in the context of the FTE structuring, evolution, and impact. An FTE observed by the Magnetospheric Multiscale mission on 2017 December 18 consisted of two flux tubes of different topology. One includes field lines with ends connected to the northern and southern hemispheres while the other includes field lines with both ends connected to the magnetosheath. Reconnection occurring at the flux-tube interface indicates how interacting flux tubes evolve into a flux rope with helical magnetic topology that is either closed or open. This study demonstrates a new aspect of how micro- to meso-scale dynamics occurring within FTEs determines their macroscale characteristics and evolution.

Unified Astronomy Thesaurus concepts: Solar-terrestrial interactions (1473); Solar-planetary interactions (1472); Solar system terrestrial planets (797); Planetary magnetospheres (997); Solar system (1528)

1. Introduction

Solar wind–magnetosphere coupling often occurs in a localized and transient manner, modifying the magnetosphere–ionosphere system of the Earth and other magnetized planets. One of the most common and important processes underlying such transient phenomena is nonsteady dayside magnetic reconnection. Contrary to continuous/quasi-steady reconnection, transient reconnection gives rise to a localized structure of enhanced magnetic flux. This structure forms and convects over the surface of the magnetosphere called the magnetopause, due to the combination of the anti-sunward magnetosheath flow and tension force exerted on the reconnected flux tube (Cooling et al. 2001). The observational evidence of such transient structures is a bipolar signature in the magnetic field component normal to the magnetopause (B_N) associated with the drifting motion (see dashed blue arrows in Figure 1(a)).

Since Russell & Elphic (1978) termed this signature a flux transfer event (FTE), numerous in situ observations have determined their typical signatures. In addition to the B_N reversal, these signatures include enhanced magnetic-field strength (B) due to a strong core field, an increase in the total pressure, and a mixture of magnetosphere and magnetosheath plasmas. These signatures have been explained by their generation via (1) localized bursty reconnection (Russell & Elphic 1978), (2) multiple X-lines (Lee & Fu 1985), or (3) temporal modulation in the single X-line reconnection process (Scholer 1988). The different generation mechanisms give rise to different magnetic-field topology and connectivity to either the northern or southern hemisphere or the magnetosheath. On the other hand, they commonly invoke formation processes occurring over macroscopic scales, resulting in FTEs with macroscale sizes comparable to one Earth radius (R_E) (Fear et al. 2007).

Recent observations using the data from the Magnetospheric Multiscale mission (MMS; Burch et al. 2016) with spacecraft separations varying from a couple of d_i (ion inertial lengths) to a few d_e (electron inertial lengths) have enabled detailed investigations of ion- or electron-scale structures and physical processes occurring within/around FTEs. The observations include evidence for (1) ion-scale secondary flux ropes (Eastwood et al. 2016; Hwang et al. 2018), (2) multilayered substructures within an FTE (Hwang et al. 2016), (3) reconnection in a compressed current sheet at the center of an FTE (Øieroset et al. 2016), and (4) reconnecting current sheet between interlinked flux tubes (IFTs; Kacem et al. 2018; Øieroset et al. 2019; Hwang et al. 2020). These observations

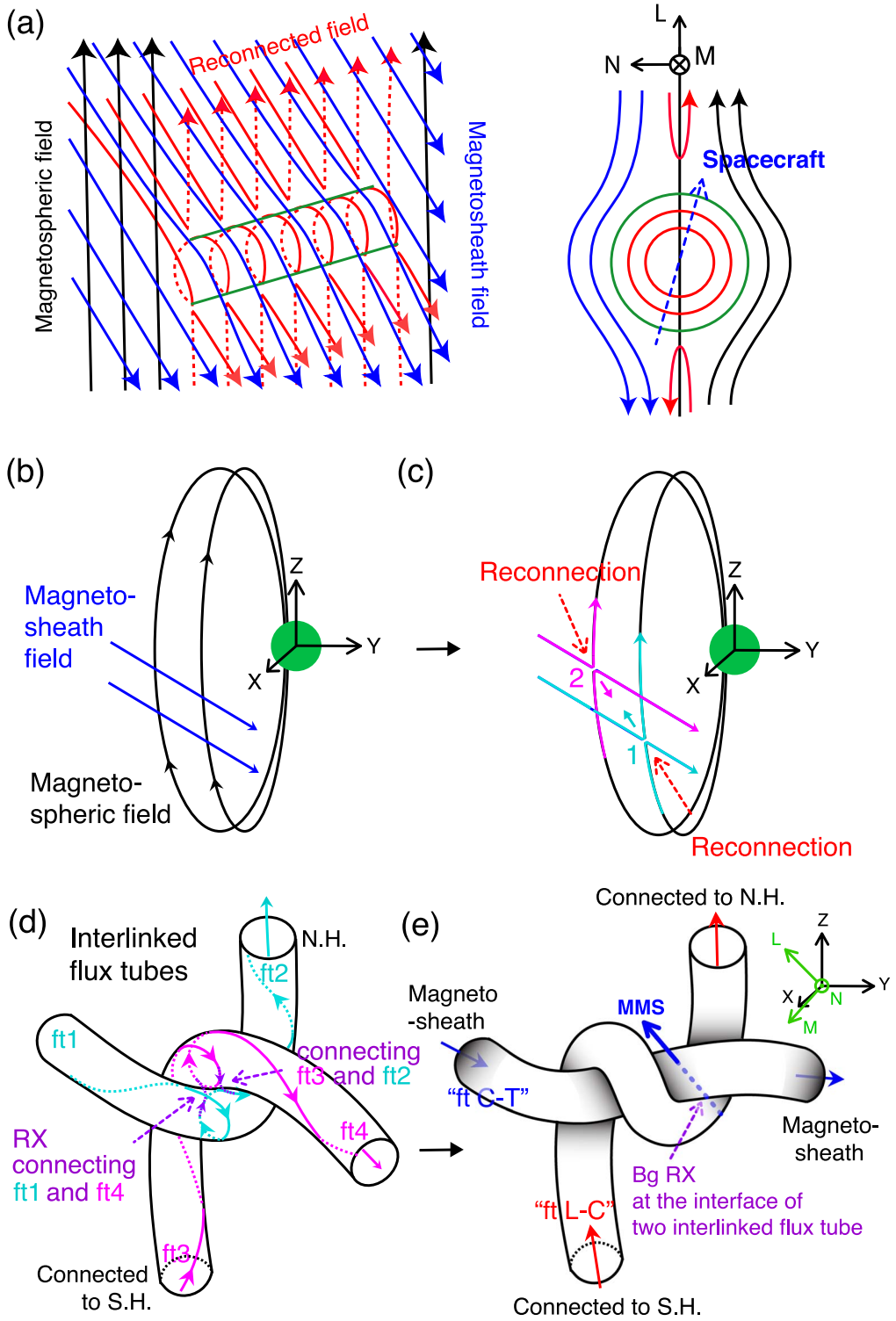

Figure 1. (a) The multiple X-line FTE model for the southward and dawnward IMF. The unreconnected magnetospheric and magnetosheath magnetic field lines are shown by black and blue arrows, respectively. Red arrows represent reconnected magnetic field lines. The edge of the FTE is shown in green. The left panel shows a view from the Sun (the normal to the magnetopause surface) and the right panel shows a view from dawn to dusk (along the direction tangential to the magnetopause). The nominal LMN coordinates for the FTE are shown at the top of the right panel. (b)–(d) Illustration of the generation of interlinked flux tubes (IFTs) under the southward and duskward IMF and (e) their connectivity to either hemisphere or both hemispheres: reconnected field lines at "1" in (c) (generating cyan field lines) can constitute a flux tube "ft1"–"ft2" in (d), with one end connected to the northern hemisphere. Reconnected field lines at "2" in (c) (generating magenta field lines) can constitute a flux tube "ft3"–"ft4," with one end connected to the southern hemisphere (d). When the interface of the interlaced flux tubes undergoes consecutive reconnection (dashed violet arrows in (d)), "ft1" and "ft4" field lines are reconnected, constituting "ft C-T" with both ends open (blue arrows in (e)), and "ft2" and "ft3" field lines are reconnected, constituting "ft L-C" with both ends connected to the magnetosphere (red arrows in (e)).

indicate that microscale (electron) and mesoscale (ion) physical processes occurring in/around FTEs play a crucial role in the generation, structure, and evolution of FTEs.

The ubiquity of reconnection occurring within FTEs has been reported (Fargette et al. 2020). The impacts of these local kinetic processes on FTE formation, structuring, and evolution,

however, have not been addressed. Yet they can be essential ingredients in the dynamics of FTEs that may grow into large-scale FTEs drifting down the tail along the magnetopause. These FTEs contribute to magnetic flux transport into the nightside magnetosphere, forming the basis of magnetospheric activities such as geomagnetic storms and substorms. Unlike the multiple X-line model (Lee & Fu 1985; see our Figure 1(a)), the IFTs and their evolution via internal reconnection within the FTE (Figures 1(d) and (e)) will suppress such transport to nightside. Thus, the localized physics occurring in FTEs may be key to understanding solar wind–magnetosphere coupling and the global magnetospheric system.

This paper presents a new aspect of kinetic processes occurring within FTEs that lead to the topological change and evolution (Figures 1(d)–(e)), implying that micro- to meso-scale dynamics inside FTEs affect the macroscale characteristics of FTEs. We use an FTE event observed by MMS to illustrate this new aspect. The detailed analyses indicate that the FTE consists of two IFTs and the kinetic process occurring at the interface of the IFTs leads to the formation of a large-scale flux rope connecting both hemispheres, therefore, potentially regulating magnetic flux transfer into the magnetotail.

2. Results

2.1. Propagation, Observation Location, and Scale Size of the Event

The MMS spacecraft was located at [9.0, −1.2, 1.3]R_E in Geocentric Solar Magnetospheric coordinates (GSM) at ∼08:15:00 UT on 2017 December 18. Figures 2 and 3 present field and particle observations by MMS over 8 s from 08:14:59 UT to 08:15:07 UT. During this period the interplanetary magnetic field (IMF) was relatively steady, pointing mostly due duskward and southward: [1.8, 8.0, −4.0] nT (not shown; see the Appendix A.1) in GSM. The tetrahedral-averaged magnetic field, i.e., interpolated value at the barycenter of the tetrahedron using the measurements at the four MMS spacecraft with an average separation of 31.6 km (Figure 2(a)) shows that B_X exhibits a bipolar signature, around which the magnetic strength (B; black) increases, indicating an FTE.

Figure 2 shows the tetrahedral-averaged measurements. Figures 3(A) and (B) show MMS4 and MMS2 observations, respectively. All vector parameters displayed in Figures 2(d)–(k) and 3 are shown in boundary normal coordinates (LMN; see the Appendix A.2): $L = [0.39, -0.61, 0.69]$, $M = [0.45, -0.52, -0.72]$, $N = [0.80, 0.60, 0.07]$ in GSM. In nominal magnetopause LMN coordinates, L mostly directs to the Earth's magnetic field along Z, and N normal to the magnetopause surface (see the top of the right panel of Figure 1(a)). For the present event, M, corresponding to the axis of an FTE, has a large fraction along Z, indicating a significant deviation of LMN from the nominal magnetopause LMN.

At ∼08:15:03.2 UT, B_N (red profile in Figures 2(d) and 3(a)) changed from negative to positive (vertical dashed black line, "C" shown on the top of Figures 2 and 3). Coincidentally, the magnetic field strength (B, black profile) increased. These magnetic perturbations are associated with the overall motion of an FTE along -L (see the dashed blue arrow in Figure 1(a)). The propagation vector of the FTE (see the Appendix A.3) was duskward and southward: [−0.45, 0.54, −0.71] in GSM or [−0.99, 0.07, −0.14] in LMN, with a speed of 204 km s^{-1}. This result is consistent with the prediction from the maximum shear model (Trattner et al. 2012, Figure 4(a)). White traces in Figure 4(a) show primary X-lines over the surface of the magnetopause when viewed from the Sun. A component reconnection X-line is located dawnward and northward of the MMS location (blue rectangle), leading to a duskward and southward motion of an FTE (black lines departing from the blue rectangle). The propagation vector (thick magenta arrow in Figure 4(a)) together with the L and M axes (black arrows) shows a good agreement between the observation and the model prediction.

We define the location where B_N becomes negative before the B_N reversal as the leading boundary of the FTE ("L" at the top of Figures 2 and 3, marked by a vertical dashed magenta line) and the region where the bipolar B_N signature ends as the trailing boundary region of the FTE ("T" at the top of Figures 2 and 3, marked by vertical cyan shades). The interval bound by "L" and "T" exhibits intense fluctuations in the current density (Figures 2(e) and (f)), including multiple peaks indicative of substructures.

The cross-sectional scale of the FTE is then estimated to be ∼756 km, which is ∼12.6 d_i (ion inertial length: ∼ 60 km for this event). The X-line located at larger L than the FTE is also evidenced by the ion velocity along -L throughout the interval (Figure 3(c)) and the ion pitch angle distribution (PAD; Figure 3(f)): when B_L fluctuated around zero between ∼"L" and "T" (Figure 3(a)), the ion flow mostly directed perpendicularly to $\boldsymbol{B}$; when B_L was negative before ∼"L" (positive around/after "T"), the ion PAD exhibited a significant parallel flux (mostly perpendicular and slightly antiparallel flux). This is consistent with thin magenta arrows in Figure 4(b) showing the MMS trajectory (dashed cyan arrow) across the FTE embedded in the southern outflow region of the X-line when viewed mostly from the -M direction.

2.2. Observation of the FTE Consisting of Two IFTs

While the B_N and B profiles suggest a typical FTE, we note a significant difference in both field and plasma signatures between before and after "C." The most invariant axis (Figure 2(b)) is primarily along X for the earlier interval ("L"–"C"), but significantly toward Y and Z for the later interval ("C"–"T"). When averaged over each interval under the error indicator (Figure 2(c)) ⩽0.5, the invariant axis directs to (−0.24, −0.38, −0.89) for "L"–"C," and (0.01, −0.83, 0.56) for "C"–"T" in LMN. The two invariant axes make an angle of 79.3°. This observation indicates that the FTE consisted of the two flux tubes (Louarn et al. 2004). Figure 4(b) shows a schematic diagram of the two flux tubes oriented almost perpendicularly. Numbers "1," "2," "3," and "4" as observed by MMS crossing the structure along the trajectory (dashed cyan arrow) correspond to a consecutive weak variation of a negative-to-positive B_L during "L"–"C" and "C"–"T," as marked by "1," "2," "3," and "4" in Figures 2(d) and 3(a).

For a force-free flux rope ($\boldsymbol{J} \times \boldsymbol{B} = 0$), the current density, $\boldsymbol{J}$ is parallel to $\boldsymbol{B}$ (Lundquist 1950). Both the curl of $\boldsymbol{B}$ ($\boldsymbol{J}$) and the curl of current-carrying, field-aligned flow vectors (flow vorticity) are predicted to be symmetric for the axial (M) component (with a single peak at the center) and bipolar for the tangential (L or N) component across the center. During ∼08:15:3.1–3.6 UT around "C," $J_{||}$ is greater than $J_{\perp}$, which, however, has a significant, nonzero value (Figure 2(f)). $\boldsymbol{J}$ (Figure 2(e)) does not follow the predicted signature. The ion

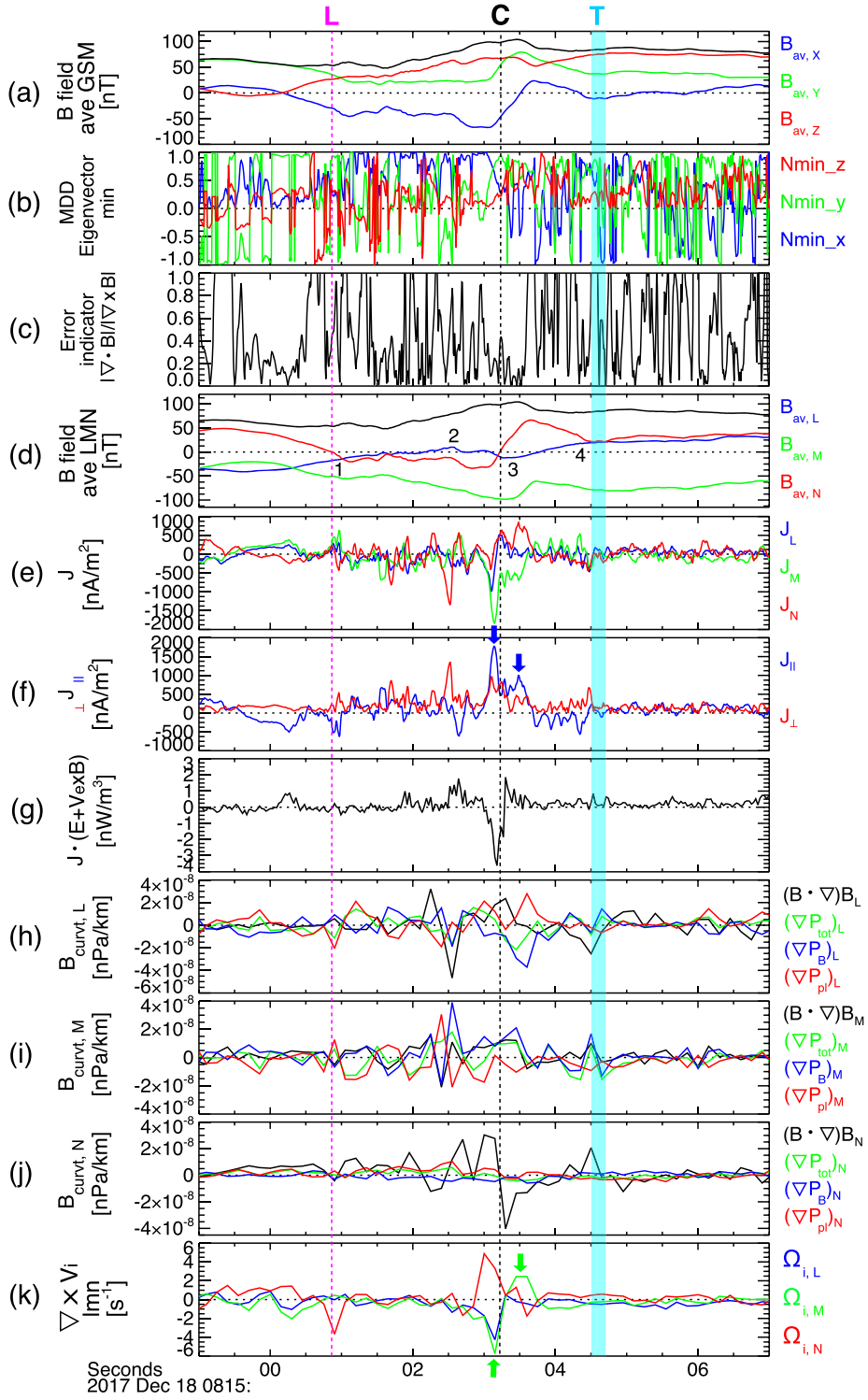

Figure 2. Four MMS observations of an FTE detected on 2017 December 18. (a) The tetrahedral-averaged magnetic field using the measurements from the four MMS spacecraft: B_X, B_Y, and B_Z components (blue, green, and red profiles) in GSM, together with the magnetic strength (B; black). (b) The result of minimum directional derivative (MDD) analysis (Siscoe & Suey 1972) showing the eigenvector of the matrix, $(\nabla \boldsymbol{B})(\nabla \boldsymbol{B})^{\mathrm{T}}$ in GSM, corresponding to the minimum eigenvalue, with an error indicator, $|\nabla \bullet \boldsymbol{B}|/|\nabla \times \boldsymbol{B}|$ (c). All vector parameters in the lower panels are shown in boundary normal coordinates, LMN that were determined from minimum variance analysis (MVA; Sonnerup & Scheible 1998) and MDD (Siscoe & Suey 1972): $L = [0.39, -0.61, 0.69]$, $M = [0.45, -0.52, -0.72]$, and $N = [0.80, 0.60, 0.07]$ in GSM. (d) The tetrahedral-averaged magnetic field ($\boldsymbol{B}$) with B_L, B_M, and B_N components (blue, green, and red profiles), together with the magnetic strength (black). (e)–(f) The current densities ($\boldsymbol{J}$; e) that are decomposed into two components (f) parallel (blue profiles; $J_{||}$) and perpendicular (red; $J_{\perp}$) to $\boldsymbol{B}$ calculated from the curlometer technique (Dunlop et al. 2002). (g) Joule dissipation in the electron rest frame, $\boldsymbol{J} \bullet \boldsymbol{E}'$, where $\boldsymbol{E}'$ is the electric field in the electron frame of reference, $\boldsymbol{E}' = \boldsymbol{E} + \boldsymbol{V}_e \times \boldsymbol{B}$. (h)–(j) The L, M, N component of the magnetic tension, $(\boldsymbol{B} \bullet \nabla \boldsymbol{B})/\mu_0$ (black) and the gradients of the total pressure ($\boldsymbol{\nabla} P_{\mathrm{tot}}$, green), the plasma pressure ($\boldsymbol{\nabla} P_{\mathrm{pl}}$, red), and the magnetic pressure ($\boldsymbol{\nabla} P_{\mathrm{B}}$, blue). (k) Ion flow vorticity ($\boldsymbol{\Omega}_i = \nabla \times \boldsymbol{V}_i$). Vertical dashed magenta, black, and cyan lines denote the leading edge, center, and trailing edge of the FTE.

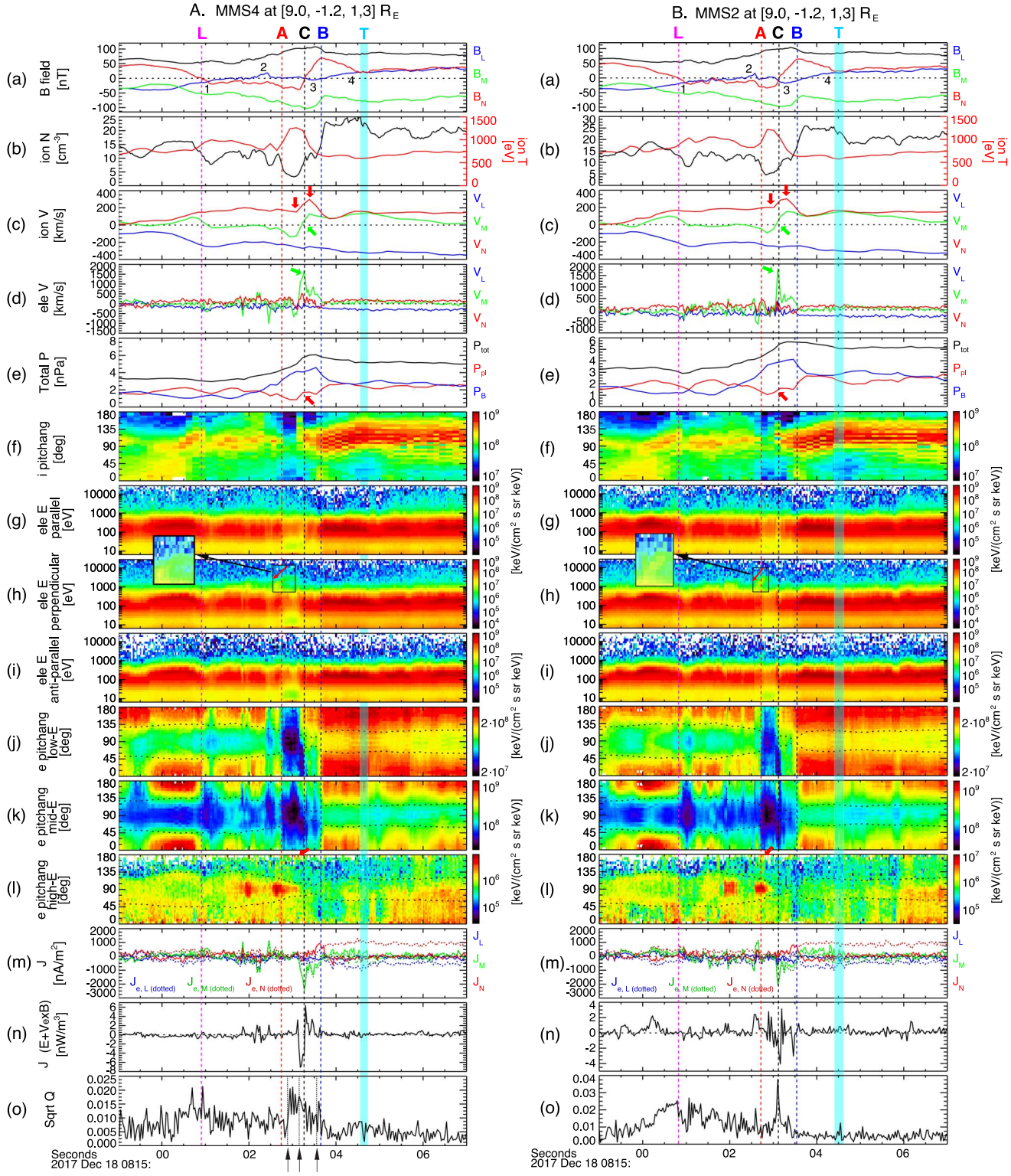

Figure 3. MMS4 (A) and MMS2 (B) observations of the FTE. (a) Magnetic field ($\boldsymbol{B}$), B_L, B_M, and B_N components (blue, green, and red profiles), together with the magnetic strength (black). (b) Ion density (black) and temperature (red). (c) Ion velocity ($\boldsymbol{V_i}$). (d) Electron velocity ($\boldsymbol{V_e}$). (e) Plasma (red) and magnetic (blue) pressures, and the sum of plasma and magnetic pressures (black). (f) Ion pitch angle distribution (PAD). (g)–(i) Energy spectrograms of electrons of parallel (0°∼30°; (g)), perpendicular (60°∼120°; (h)), and antiparallel (150°∼180°; (i)) pitch angles. (j)–(l) Pitch angle distributions (PADs) of the low- (∼10 eV ⩽energy <100 eV; (j)), mid- (100 eV ⩽energy <1 keV; (k)), and high- (1 keV ⩽energy <26 keV; (l)) energy electrons. (m) The current densities obtained from the particle data (solid lines) with the current densities carried by electrons only (dotted). (n) Joule dissipation in the electron rest frame, $\boldsymbol{J}\bullet\boldsymbol{E}'$, using the single spacecraft data. All vector parameters are shown in LMN coordinates. (o) $\sqrt{Q}$ quantifying the level of departures from gyrotropy using electron pressure tensors (Swisdak 2016): 0 for gyrotropic tensors and 1 for maximal departures from gyrotropy. Vertical dashed magenta, black, and cyan lines denote the leading edge, center, and trailing edge of the FTE. Vertical dashed red and black lines mark the location where abrupt changes in the low- and mid-energy electron fluxes (Figures 3(j) and(k)) appear.

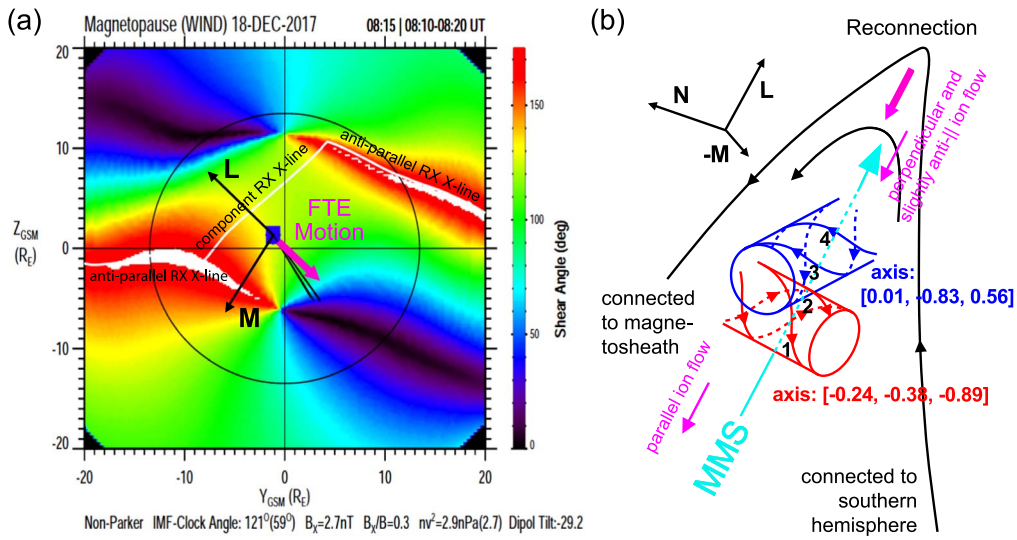

Figure 4. Modeled shear angles between the magnetosheath and magnetospheric magnetic field lines using the solar wind IMF condition and Earth's dipole tilt for the event shown in Figures 2 and 3. Black arrows indicate LMN coordinates for the present event that deviated from nominal magnetopause LMN. White traces represent primary X-lines over the surface of the magnetopause when viewed from the Sun. A blue rectangle denotes the location of the MMS spacecraft. Black lines and a thick magenta arrow show the model prediction and the observation, respectively, of the plasma bulk flow or the motion of the FTE observed at the MMS location. (b) A schematic diagram of the FTE structure consisting of two interlinked flux tubes (IFTs) embedded in the southern outflow region of the reconnection X-line when viewed mostly from the -*M* direction.

vorticity (Figure 2(k)) shows an opposite trend: bipolar $\Omega_{i,M}$ and relatively symmetric $\Omega_{i,N}$ across ∼"C." $J_{||}$ shows double peaks around "C," instead of a single peak (blue arrows in Figure 2(f)). These peaks coincide with bipolar peaks in $\Omega_{i,M}$ (green arrows in Figure 2(k)). The *L*-directional magnetic tension (Figure 2(h)) that is expected to be bipolar across "C," exhibits complicated profiles. These observations further support that the present FTE is not a single force-free flux-rope FTE.

Plasma parameters also show notable differences across "C": ion density (temperature) is lower (higher) during "L"–"C" than "C"–"T" (Figure 3(b)); $V_{i,M}$ changes from negative to positive across "C" (green arrows in Figure 3(c)). The electron PAD exhibits dramatic changes across "C" and the variations are energy-dependent: the low- and mid-energy electron fluxes (Figures 3(j) and (k)) are lower during "L"–"C" than "C"–"T," including a significant reduction immediately before ∼"C" during "A"–∼"L" (see the top of Figures 3(A) and (B)). These low- (and mid-) energy electrons are mostly counter-streaming during "L"–"C" while low-energy electrons are mostly one-directional (antiparallel) immediately after ∼"C" during ∼"L"–"B." Most importantly, 90°-pitch-angle electrons are greatly enhanced in the high-energy range only before "C" (Figure 3(l)). They are likely to be trapped on the closed magnetospheric field lines (supported by the low-density and high-temperature plasma; Figure 3(b); to be discussed below). The reduction of such 90°-focused populations during "C"–"T" indicates newly opened magnetosheath field lines or open field lines that allow hot magnetospheric populations to escape. These significant differences in the electron PAD indicating completely different magnetic connectivity across "C" strongly supports the interpretation of two IFTs, instead of a single flux-rope-type FTE (such as Figure 1(a)).

2.3. Reconnection at the Interface of Two IFTs

Around "C," *B* (black profile in Figure 3(a)) and the magnetic pressure (P_B; blue in Figure 3(e)) display a suppressed peak. This is a so-called "M"-shaped crater FTE (Labelle et al. 1987). The plasma pressure (P_{pl}; red arrows in Figure 3(e)) was locally enhanced at "C." These P_B and P_{pl} variations constitute a relatively single P_{tot} (the total pressure; black profiles in Figure 3(e)) enhancement around "C."

The *B* suppression at "C" might result from local reconnection. This is supported by the existence of an abrupt change in B_N (rather than sinusoidal bipolar B_N), indicating a local current sheet (red profile in Figures 2(d) and 3(a)). (Note that the present *L*, *M*, and *N* axes correspond to *N*, −*M*, and *L* axes, respectively, in nominal 2D reconnection current-sheet geometry, where *L* directs along the current sheet and *N* points to the current sheet normal.) Correspondingly, ion outflow jets directed along the current sheet, *N* (red arrows in Figure 3(c)). Out-of-plane electron jets along *M* (vertical green arrow in Figure 3(d)) carried the electric current during ∼"A"–"B" with a peak at "C" (dotted profiles in Figure 3(m) that show the current densities carried by electrons, only), as observed in the electron diffusion region (EDR; Torbert et al. 2018). Joule dissipation in the electron rest frame, $\boldsymbol{J}\bullet\boldsymbol{E}'$ fluctuated, showing negative values before/around "C" (Figure 3(n)). These observations are consistent with large guide-field reconnection signatures (Eriksson et al. 2016; Nakamura et al. 2017). The positive $\boldsymbol{J}\bullet\boldsymbol{E}'$ represents an energy transfer from $\boldsymbol{B}$ to plasma, as expected for reconnection. The highly fluctuating $\boldsymbol{J}\bullet\boldsymbol{E}'$ indicates strong interactions between $\boldsymbol{B}$ and plasma with the negative values implying the outer edge of the EDR (Hwang et al. 2017) or associations with waves in/near the EDR (Swisdak et al. 2018; Burch et al. 2020).

Figure 5 shows electron distribution functions (f_e) at three selected times before, around, and after "C" (Figures 5(a), (b), and (c)), denoted by black arrows at the bottom of Figure 3(A). The upper and lower panels show f_e in plane containing $\boldsymbol{B}$ ($\boldsymbol{V_B}$) and $\boldsymbol{V}_{\perp 1} = \boldsymbol{B} \times (\boldsymbol{V}_i \times \boldsymbol{B})$, where $\boldsymbol{V_i}$ is the ion bulk velocity (upper) and in plane perpendicular to $\boldsymbol{B}$ with $\boldsymbol{V}_{\perp 1}$ and $\boldsymbol{V}_{\perp 2} = \boldsymbol{B} \times \boldsymbol{V}_i$ (lower).

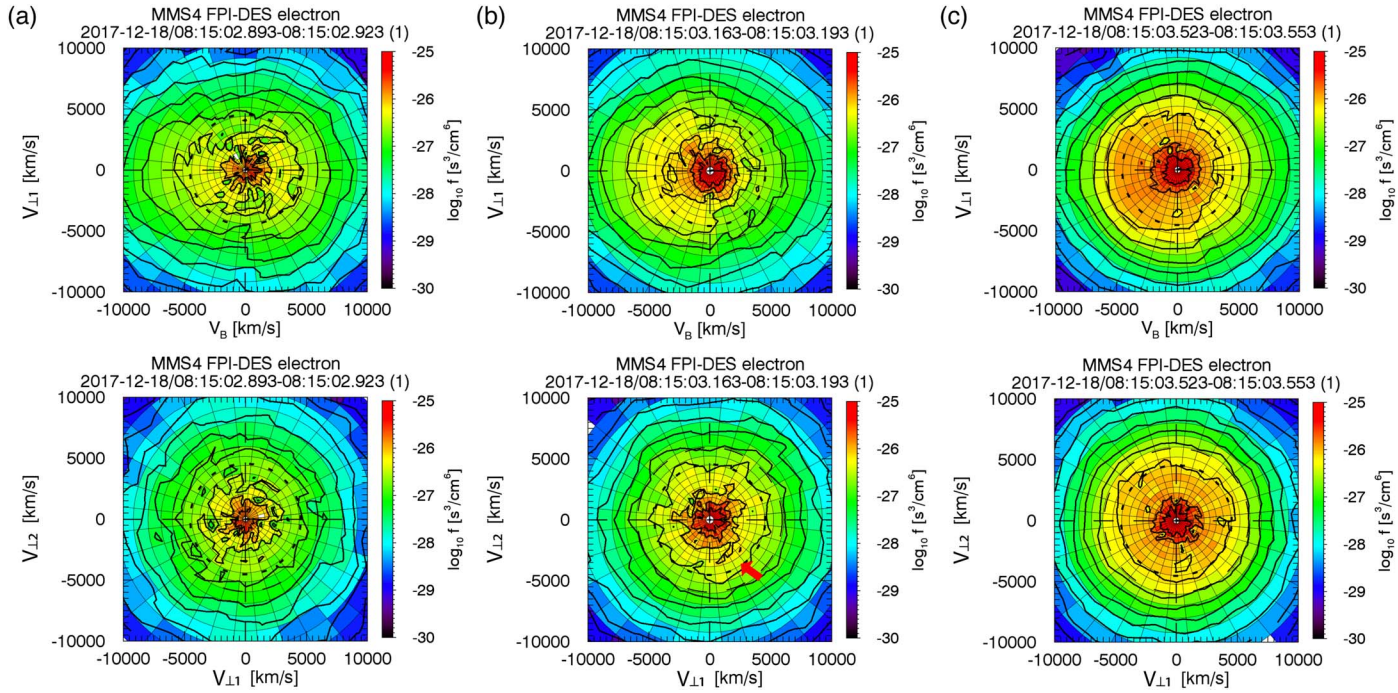

Figure 5. MMS4 observations of 2D cuts of 3D electron distributions (integrated over ±11.25° from the cut) at three selected times before, around, and after the center of FTE ((a), (b), and (c)), denoted by black arrows at the bottom of Figure 3(A). The upper and lower panels show the electron distributions as a function of ($V_{||}$, $V_{\perp 1}$) and ($V_{\perp 1}$, $V_{\perp 2}$), respectively. Parallel and perpendicular directions are defined with respect to the local magnetic field ($\boldsymbol{B}$). The two perpendicular directions are chosen to be perpendicular to $\boldsymbol{B}$ approximately along the ion bulk velocity ($\boldsymbol{V_i}$), $\boldsymbol{V}_{\perp 1} = \boldsymbol{B} \times (\boldsymbol{V}_{\rm i} \times \boldsymbol{B})$ and $\boldsymbol{V}_{\perp 2} = \boldsymbol{B} \times \boldsymbol{V}_{\rm i}$. A lack of axisymmetry in the ($V_{\perp 1}$, $V_{\perp 2}$) distribution is denoted by a red arrow in the lower middle panel in comparison to the lower left and right panels showing almost gyrotropic distributions.

Figure 5(a) shows low-density, high-temperature (Figure 3(b)) magnetospheric electrons. Figure 5(c) shows heated, antiparallel-streaming magnetosheath electrons. Figure 5(b) shows a mixture of the two populations. The superposition of a magnetosheath population is shaped as a half shell in the ($-V_{\rm B}$, $V_{\perp 1}$) plane. Simultaneously, $f_{\rm e}(V_{\perp 1}, V_{\perp 2})$ shows a certain level of agyrotropy, i.e., a lack of axisymmetry (red arrow in the lower middle panel). Figure 3(o) shows $\sqrt{Q}$ that quantifies the level of agyrotropy (Swisdak 2016): 0 for gyrotropy; 1 for maximal agyrotropy. $\sqrt{Q}$ is enhanced around "C" (MMS4) or peaks at "C" (MMS2). The half-shell shape in $f_{\rm e}(V_{\rm B}, V_{\perp})$ together with a weak agyrotropy indicates the outer edge of the EDR (Hwang et al. 2017). These simultaneous observations of B_N reversal, ion outflow jets, out-of-plane electron jets, nonzero $\boldsymbol{J}\bullet\boldsymbol{E}'$, and half-shell/slightly agyrotropic distribution manifest that reconnection was occurring in the interface between two IFTs.

3. Discussion

Our analyses indicate that the present FTE consisted of two IFTs and reconnection was occurring at the interface of these flux tubes. We discuss the origin of the 90°-focused high-energy electrons exclusively observed before "C" (Figure 3(l)) and force analysis. These suggest a global picture of the FTE, including its evolution and effect on solar wind–magnetosphere coupling.

3.1. Magnetic Topology of Two IFTs

The 90°-focused energetic electrons can be either locally energized or trapped on the field lines connected to both hemispheres. The former corresponds to electrons locally bouncing within the exhaust region with a large magnetic gradient/curvature, showing a pitch-angle broadening at B-minima in accordance with the first adiabatic invariant (Hwang et al. 2018). We overplotted black dotted contours in Figures 3(j)–(l) that represent loss-cone angles, assuming that there is a mirror point with a magnetic strength of 107.7 nT (the maximum B for MMS4; Figure 3(A)) or 104.1 nT (MMS2; Figure 3(B)). These contours generally separate the 90°-focused population from field-aligned (<∼45°) and weaker antiparallel (>∼135°) populations (Figure 3(l)). This signature is, however, mostly seen before "C," during which the pitch-angle broadening often shows a deviation from the expectation. Furthermore, the locally bouncing/focusing population will result in a balance in fluxes between parallel and antiparallel components. The parallel population prevails over the antiparallel throughout the period (compare Figures 3(g) and (i)). There is also an interval during which the antiparallel population is more dominant (red arrows at the top of Figure 3(l)). Although the former can be related to the overall structure embedded in the southern outflow region of an X-line (Figure 4(b)), the latter is hardly explained. Thus, the local energization cannot explain these 90°-focused electrons that were exclusively observed before "C" and accompanied by the imbalanced parallel and antiparallel fluxes.

For electrons being trapped on the field lines with their ends connected to the northern and southern hemispheres, it takes ∼5 s (2 s) for 1 keV (10 keV) electrons to travel 5 R_E along the magnetopause field lines. The most energetic electrons on recently closed field lines (via reconnection at the interface of the IFTs) will constitute the 90°-focused population, while less energetic electrons will lead to the imbalance between the parallel and antiparallel fluxes. On the other hand, the most energetic electrons on early-closed field lines escape away from the field lines, while less energetic ones remain trapped at 90°. This feature is exactly seen as an inverse

energy-time dispersion of high-energy electrons with perpendicular pitch angles (red arrows and inlets expanding black rectangles in Figure 3(h)).

The reduction of the 90°-focused energetic electrons after "C" indicates newly opened magnetosheath field lines or open field lines with one end connected to the northern or southern hemisphere (Figure 3(l)). During "C"–"T," the parallel high-energy population was still denser than the antiparallel one, possibly due to the background effect associated with the location of the overall structure. Before/around "B," a notable reduction in these energetic electrons, together with uni/bidirectional low-energy electrons (Figure 3(j)) indicates the magnetosheath field lines (with neither end connected to the hemisphere), on which the low-energy magnetosheath electrons flow along one direction or both directions along $\boldsymbol{B}$.

Thus, the two flux tubes across "C" contain field lines of different magnetic topologies: one with the field lines connected to both hemispheres and the other with open field lines connected to the magnetosheath. This was further evidenced by the plasma density and temperature (Figure 3(b)) and f_e (Figure 5). Russell & Qi (2020) indicates the ubiquity of such paired flux tubes.

Figures 1(b)–(e)) illustrate the generation of such IFTs and diverse connectivity. For the southward and duskward IMF during this event (Figure 1(b)), reconnected field lines at "1" in Figure 1(c) (generating cyan field lines) constitute a flux tube "ft1"–"ft2" (Figure 1(d)), with one end connected to the northern hemisphere. Reconnected field lines at "2" in Figure 1(c) (generating magenta field lines) constitute a flux tube "ft3"–"ft4," with one end connected to the southern hemisphere (Figure 1(d)). When the interface of the IFTs undergoes reconnection (dashed violet arrows in Figure 1(d)), "ft1" and "ft4" field lines are reconnected, constituting "ft C-T" with both ends connected to the magnetosheath (blue arrows in Figure 1(e)), and "ft2" and "ft3" field lines are reconnected, constituting "ft L-C" with both ends connected to the magnetosphere (red arrows in Figure 1(e)). When these newly IFTs move southward/duskward past by MMS as depicted by a blue arrow in Figure 1(e) mostly along L, "ft L-C" is first traversed by MMS, then, "ft C-T" is traversed, consistent with the observations of Figure 4(b) and the electron PADs.

We note that the reconnecting flux tubes (Figure 1(d)) result in a more complicated structure (Figure 1(e)). While reconnection locally releases the magnetic energy to particles, it can induce a higher magnetic-energy state for a larger-scale structure due to original magnetic topology/connectivity of the field lines that were involved in the reconnection process, similar to Figure 1(d) having higher magnetic energy structure than Figure 1(c). The resulting structure (Figure 1(e)) will exert strong magnetic tension force toward the interface of the IFTs. This facilitates an interaction of the interface, e.g., reconnection at this interface (dashed violet arrows in Figure 1(e)), which was observed by MMS (Section 2). The magnetic tension, $(\boldsymbol{B}\bullet\nabla\boldsymbol{B})_N/\mu_0$ (black profiles in Figure 2(j)) reverses its sign from positive to negative across "C," as expected for "ft L-C" and "ft C-T" in Figure 1(e). The strong, clearly bipolar feature across "C," thus, supports the complicated IFTs (Figure 1e). (Note that in Figure 1(d) each flux tube has one fixed end connected to either the northern or southern hemisphere. This can result in a (significant) bipolar magnetic tension component along L, which is not shown in this event (Figure 2(h)).) Also note that "ft C-T" that is connected to the magnetosheath on both ends will be dragged in the antisunward direction by the magnetosheath flow enhancing the N component of the magnetic tension force.

The present event cannot be interpreted as ripples on the magnetopause caused by a wave or passing FTE that can locate MMS from the magnetosphere to the magnetosheath. It is because neither interval before/after "C" represents a preexisting magnetospheric or magnetosheath region. The inverse dispersion of the 90°-focused electrons and the imbalance between parallel and antiparallel fluxes before "C" are hardly explained without invoking newly reconnected/closed field lines. The existing, although weak, energetic flux after "C" indicates newly opened magnetosheath field lines. The bipolar $(\boldsymbol{B}\bullet\nabla\boldsymbol{B})_N/\mu_0$ across "C" and reconnection observed at ∼"C" support that the two regions were interlinked and interacting.

An FTE is force-balanced when $(\boldsymbol{B}\bullet\nabla\boldsymbol{B})/\mu_0$ is equal to $\nabla P_{\rm tot}$, and is force-free when $(\boldsymbol{B}\bullet\nabla\boldsymbol{B})/\mu_0$ is equal to $\nabla P_{\rm B}$. $(\boldsymbol{B}\bullet\nabla\boldsymbol{B})_N/\mu_0$ (N -directional magnetic tension; black profiles in Figure 2(j)) is not balanced by any of the pressure gradients (red, blue, and green profiles in Figure 2(j)). The L and M components (black profiles in Figure 2(h) and (i)) are partly balanced by $\nabla P_{\rm tot}$ (green) or $\nabla P_{\rm B}$ (blue). Around "C," $J_{||}$ is larger than $J_{\perp}$, which is, however, significant (Figure 2(f)). These suggest that the FTE is neither force-free nor force-balanced. This might indicate that the FTE was under evolution, explaining the highly variable plasma flows (Figure 3(c), (d)), $\boldsymbol{J}$ (Figure 2(e) and (f); Figure 3(m)), and $\boldsymbol{J}\bullet\boldsymbol{E}'$ (Figure 2(g); Figure 3(n)). Depending on the evolutionary phase of IFTs, a portion of field lines can be either connected to one hemisphere (Figure 1(d)) or both hemispheres (Figure 1(e)).

3.2. Implications and Conclusion

The complex magnetic-field topology and various magnetic connectivity within the FTE result from the kinetic process, i.e., reconnection locally occurring at the FTE center (not occurring outside or at the periphery of the FTE). This makes a striking distinction from the previous multiple X-line FTE model (Lee & Fu 1985; see our Figure 1(a)) that can also involve newly opened magnetosheath fields or completely closed fields (Pu et al. 2013). When connected to both hemispheres, the flux tube becomes an efficient channel for solar wind transfer into the magnetosphere. The resulting structure (Figure 1(e)) resembles a typical flux-rope structure, and consecutive interface reconnection will lead further evolution to a flux rope (twining flux tubes). Such interlinking will suppress magnetic-flux transfer into the magnetotail, via which FTEs act for the main driver of the magnetospheric dynamics such as substorms/storms (Fear et al. 2017). The magnetic connectivity will continuously vary during different epochs in the evolution, both regulating the transfer of the solar wind into the magnetosphere and the magnetic flux transfer from the dayside to the magnetotail.

The importance of the kinetic processes occurring inside FTEs is, therefore, twofold. First, they lead to the topological structure and evolution of FTEs. Second, they determine macroscale characteristics of FTEs (magnetic connectivity and magnetic content), including their global effects. The present event implies that such a kinetic process can play a crucial role in the generation, structure, evolution, and impact of FTEs.

This study was supported, in part, by NASA's MMS project at SwRI, NSF AGS-1834451, NASA 80NSSC18K1534, 80NSSC18K0570, 80NSSC18K0693, 80NSSC18K1337, 80NSSC18K0657, and ISSI program: MMS and Cluster observations of magnetic reconnection. MMS data sets were provided by the MMS science working group teams through the link (http://lasp.colorado.edu/mms/sdc/public/). The ARTEMIS data are available at http://themis.ssl.berkeley.edu. K.J.H. thanks and acknowledges MMS instrument teams for providing data.

Appendix

A.1. Instrumentation and Data Availability

The MMS spacecraft (Burch et al. 2016) flying in low-inclination and highly elliptical orbits provide the measurements at/near Earth's magnetopause, bow show, and magnetotail. The four spacecraft are identically equipped with instruments including plasma instruments (FPI; Pollock et al. 2016), magnetometers (FGM; Russell et al. 2016), and electric field instruments (EDP) consisting of the spin-plane double probe (SDP; Lindqvist et al. 2016) and the axial double probe (ADP; Ergun et al. 2016). We used the magnetic field data from FGM with a time resolution of 10 ms in burst mode, the DC electric field data with a 0.122 ms time resolution in burst mode, and particle data in burst mode from the FPI/DIS (Dual Ion Spectrometer) for ions and FPI/DES (Dual Electron Spectrometer) for electrons with a 150 and 30 ms time resolution, respectively, a $11\overset{\circ}{.}25$ angular resolution, and an energy range of ~10 eV–26 keV. The MMS data are accessible through the public link provided by the MMS science working group teams: http://lasp.colorado.edu/mms/sdc/public/.

The Moon-orbiting Acceleration, Reconnection, Turbulence and Electrodynamics of the Moon's Interaction with the Sun (ARTEMIS) spacecraft (Angelopoulos 2011), designed to investigate the Moon's interaction with the solar wind, also provide high time resolution (3 s) data of solar wind conditions. For the present study we use the data from the fluxgate magnetometer (FGM) and electrostatic analyzer to obtain interplanetary magnetic field (IMF) orientation and solar wind speed for the present FTE event. The ARTEMIS data are available at http://themis.ssl.berkeley.edu/. The data were lagged by 13 minutes in this event to account for the transit time of the solar wind from ARTEMIS P2, located at [64.2, 3.3, 3.3]R_E in GSM to MMS at [9.0, −1.2, 1.3]R_E in GSM.

A.2. Determination of Boundary Normal Coordinates (LMN)

We determined boundary normal coordinates (LMN) by performing (1) minimum variance analysis (MVA; Sonnerup & Scheible 1998) and (2) minimum directional derivative (MDD) analysis (Siscoe & Suey 1972). The former method using the four-spacecraft magnetic field data during 0815:01.0–04.5 UT derived $L = [0.35, -0.72, 0.60]$, $M = [0.46, -0.43, -0.78]$, and $N = [0.82, 0.55, 0.17]$ in GSM. To comply with conventions, N points outward from the magnetopause and L points northward along the dayside magnetopause, partly aligning the magnetospheric magnetic field (see the top of the right panel of Figure 1(a)). The medium-to-minimum (maximum-to-medium) eigenvalue ratio was ~3.3 (4.5), indicating a relatively reliable calculation (Shi et al. 2005). The MDD result is shown in Figures 2(b)–(c). The eigenvector of the matrix, $(\nabla \boldsymbol{B})(\nabla \boldsymbol{B})^{\mathrm{T}}$ corresponding to the minimum eigenvalue significantly fluctuated (Figure 2(b)). At ~0815:03.5 UT, around which the sign of B_X was reversed (Figure 2(a)) and the error was minimized (Figure 2(c)), the three eigenvectors of $(\nabla \boldsymbol{B})(\nabla \boldsymbol{B})^{\mathrm{T}}$ pointed $L = [0.39, -0.61, 0.69]$, $M = [0.45, -0.52, -0.72]$, and $N = [0.80, 0.60, 0.07]$ in GSM, where M corresponds to the (negative/positive) eigenvector for the minimum eigenvalue of $(\nabla \boldsymbol{B})(\nabla \boldsymbol{B})^{\mathrm{T}}$ (Figure 2(b)), representing the most invariant axis. The difference between MVA-derived and MDD-derived L, M, and N ranged from $5\overset{\circ}{.}8$ to $8\overset{\circ}{.}3$. We used the averaged MVA and MDD result: $L = [0.38, -0.66, 0.65]$, $M = [0.46, -0.48, -0.75]$, and $N = [0.81, 0.58, 0.12]$ in GSM.

A.3. Determination of the Propagation Velocity of the Observed FTE Structure

To investigate the propagation of the FTE, we performed multiple triangulation analysis (Zhou et al. 2006) using a four-spacecraft timing analysis (Paschmann et al. 1998).

ORCID iDs

K.-J. Hwang https://orcid.org/0000-0001-9583-8882
J. L. Burch https://orcid.org/0000-0003-0452-8403
C. T. Russell https://orcid.org/0000-0003-1639-8298
K. Dokgo https://orcid.org/0000-0003-3917-7885
S. A. Fuselier https://orcid.org/0000-0003-4101-7901
H. Hasegawa https://orcid.org/0000-0002-1172-021X
H. Fu https://orcid.org/0000-0002-4701-7219
Y. Khotyaintsev https://orcid.org/0000-0001-5550-3113
D. B. Graham https://orcid.org/0000-0002-1046-746X
D. J. Gershman https://orcid.org/0000-0003-1304-4769
R. E. Ergun https://orcid.org/0000-0002-3096-8579
R. B. Torbert https://orcid.org/0000-0001-7188-8690
J. Broll https://orcid.org/0000-0002-9139-5495

References

Angelopoulos, V. 2011, SSRv, 165, 3
Burch, J. L., Moore, T. E., Tobert, R. B., & Giles, B. L. 2016, SSRv, 199, 5
Burch, J. L., Webster, J. M., Hesse, M., et al. 2020, GeoRL, 47, 1
Cooling, B. M. A., Owen, C. J., & Schwartz, S. J. 2001, JGRA, 106, 18763
Dunlop, M. W., Balogh, A., Glassmeier, K.-H., & Robert, P. 2002, JGRA, 107, 1384
Eastwood, J. P., Phan, T. D., Cassak, P. A., et al. 2016, GeoRL, 43, 4716
Ergun, R. E., Tucker, S., Westfall, J., et al. 2016, SSRv, 199, 167
Eriksson, S., Wilder, F. D., Ergun, R. E., et al. 2016, PhRvL, 117, 015001
Fargette, N., Lavraud, B., Øieroset, M., et al. 2020, GeoRL, 47, e86726
Fear, R. C., Milan, S. E., Fazakerley, A. N., et al. 2007, AnGeo, 25, 1669
Fear, R. C., Trenchi, L., Coxon, J. C., & Milan, S. E. 2017, JGRA, 122, 12310
Hwang, K. J., Dokgo, K., Choi, E., et al. 2020, JGRA, 125, e27665
Hwang, K. J., Sibeck, D. G., Burch, J. L., et al. 2018, JGRA, 123, 8473
Hwang, K. J., Sibeck, D. G., Choi, E., et al. 2017, GeoRL, 44, 2049
Hwang, K. J., Sibeck, D. G., Giles, B. L., et al. 2016, GeoRL, 43, 9434
Kacem, I., Jacquey, C., Génot, V., et al. 2018, JGRA, 123, 1779
Labelle, J., Treumann, R. A., Haerendel, G., et al. 1987, JGRA, 92, 5827
Lee, L. C., & Fu, Z. F. 1985, GeoRL, 12, 105
Lindqvist, P. A., Olsson, G., Torbert, R. B., et al. 2016, SSRv, 199, 137
Louarn, P., Fedorov, A., Budnik, E., et al. 2004, GeoRL, 31, L19805
Lundquist, S. 1950, Magnetohydrostatic fields, Ark. Fys, 2, 361
Nakamura, T. K. M., Hasegawa, H., Daughton, W., et al. 2017, NatCo, 8, 1
Øieroset, M., Phan, T. D., Drake, J. F., et al. 2019, GeoRL, 46, 1937
Øieroset, M., Phan, T. D., Haggerty, C., et al. 2016, GeoRL, 43, 5536
Paschmann, G., Daly, P. W., Robert, P., et al. 1998, Analysis Methods for Multi-Spacecraft Data (Bern: ISSI) SR-001
Pollock, C., Moore, T., Jacques, A., et al. 2016, SSRv, 199, 331
Pu, Z. Y., Raeder, J., Zhong, J., et al. 2013, GeoRL, 40, 3502
Russell, C. T., Anderson, B. J., Baumjohann, W., et al. 2016, SSRv, 199, 189
Russell, C. T., & Elphic, R. C. 1978, SSRv, 22, 681
Russell, C. T., & Qi, Y. 2020, GeoRL, 47, 1
Scholer, M. 1988, GeoRL, 15, 291
Shi, Q. Q., Shen, C., Pu, Z. Y., et al. 2005, GeoRL, 32, L12105

Siscoe, G. L., & Suey, R. W. 1972, JGRA, 77, 1321
Sonnerup, B., & Scheible, M. 1998, in Analysis Methods for Multi-Spacecraft Data, Minimum and Maximum Variance Analysis, Vol. 43, ed. P. W. Daly (ISSI: Bern), 249
Swisdak, M. 2016, GeoRL, 43, 43
Swisdak, M., Drake, J. F., Price, L., et al. 2018, GeoRL, 45, 5260
Torbert, R. B., Burch, J. L., Phan, T. D., et al. 2018, Sci, 362, 1391
Trattner, K. J., Petrinec, S. M., Fuselier, S. A., & Phan, T. D. 2012, JGRA, 117, A01213
Zhou, X. Z., Zong, Q. G., Wang, J., et al. 2006, AnGeo, 24, 3173